Proceedings World Geothermal Congress 2020+1
Reykjavik, Iceland, April - October 2021

A Numerical Model for Formation Dry-out During CO_{2n} Injection in Fractured Reservoirs Using the MOOSE Framework: Implications for CO_2-based Geothermal Energy Extraction

M. M. Grimm Lima[1], P. Schädle, D. Vogler, M.O. Saar, X.-Z. Kong[2]

Geothermal Energy and Geofluids Group, Institute of Geophysics, ETH Zürich, Sonneggstrasse 5, 8092 Zürich, Switzerland
([1]marinbra@ethz.ch and [2]xkong@ethz.ch)

Keywords: Formation dry-out, Fractured reservoirs, CO_2 injection, Salt precipitation, Permeability impairment, MOOSE numerical framework, CO_2-geothermal

ABSTRACT

Injection of supercritical carbon dioxide ($scCO_2$) into geological reservoirs is involved in Carbon Capture, Utilization, and Storage (CCUS), such as geological CO_2 storage, and Enhanced Geothermal Systems (EGS). The potential physico-chemical interactions between the dry $scCO_2$, the reservoir fluid, and rocks may cause formation dry-out, where mineral precipitates due to continuous evaporation of water into the $scCO_2$ stream. This salt precipitation may impair the rock bulk permeability and cause a significant decrease in the well injectivity. Formation dry-out and the associated salt precipitation during $scCO_2$ injection into porous media have been investigated in previous studies by means of numerical simulations and laboratory experiments. However, few studies have focused on the dry-out effects in fractured rocks in particular, where the mass transport is strongly influenced by the fracture aperture distribution. In this study, we numerically model the dry-out processes occurring during $scCO_2$ injection into brine-saturated single fractures and evaluate the potential of salt precipitation. Fracture aperture fields are photogrammetrically determined with fracture geometries of naturally fractured granite cores from the Deep Underground Geothermal (DUG) Lab at the Grimsel Test Site (GTS), in Switzerland. We use an open-source, parallel finite element framework to numerically model two-phase flow through a 2D fracture plane. Under in-situ reservoir conditions, the brine is displaced by dry $scCO_2$ and also evaporates into the CO_2 stream. The fracture permeability is calculated with the local cubic law. Additionally, we extend the numerical model by the Young-Laplace equation to determine the aperture-based capillary pressure. Finally, as future work, the precipitation of salt will be modelled by employing a uniform mineral growth approach, where the local aperture uniformly decreases with the increase in precipitated mineral volume. The numerical simulations assist in understanding the long-term behaviour of reservoir injectivity during subsurface applications that involve $scCO_2$ injection, including CO_2-based geothermal energy extraction.

1. INTRODUCTION

Injection of supercritical carbon dioxide ($scCO_2$) into geological reservoirs is involved in Carbon Capture, Utilization, and Storage (CCUS), such as geological CO_2 storage, and Enhanced Geothermal Systems (EGS). More specifically, in the context of EGS projects, CO_2 has been proposed as an alternative heat transmission fluid, due to its greater buoyancy and lower viscosity compared to water (Brown, 2000; Pruess 2006). In EGS applications, $scCO_2$ is injected into brine-saturated reservoirs, which are often tight rocks, where permeability is significantly higher in fractures than in the rock mass. While the thermal and hydraulic aspects of $scCO_2$-EGS systems are encouraging, the potential chemical and physical interactions between the dry $scCO_2$, reservoir fluid and rocks may cause precipitation of salt within the fluid filled void space, which is also known as subflorescence (Shahidzadeh-Bonn et al., 2010). This subflorescence of salt is the result of continuous mass transfer of water from the aqueous phase into the CO_2-rich phase, in a process called formation dry-out. Depending on the distribution of the mineral (e.g. NaCl) precipitate within the pore space, the salt can significantly impair reservoir injectivity (Muller et al., 2009) and can compromise the long-term operation of $scCO_2$-based EGS projects.

Several field observations of injectivity impairment, caused by mineral precipitation, have been reported in injection wells in natural gas (Golghanddashti et al., 2013) and CO_2 (Baumann et al., 2014) storage operations in saline aquifers, and during injection/production from gas reservoirs (Kleinitz et al., 2001; Maxwell and Young, 2014). For example, salt precipitation was attributed to be partially the cause of the extra pressure buildup observed in the injection wells of the Ketzin and Snöhvit projects, which investigated CO_2 storage in saline sandstone aquifers (Hansen et al., 2013; Baumann et al., 2014). In an attempt to better predict these injectivity variations, formation dry-out and associated salt precipitation during $scCO_2$ injection into porous media have been investigated by means of numerical simulations (Giorgis et al., 2007; Müller et al., 2009; Ott et al., 2011; André et al., 2014; Roels et al., 2014), analytical models (Pruess and Garcia, 2002; Pruess and Müller, 2009; Peysson, 2012), and laboratory experiments (Ott et al., 2011, Peysson, 2012; Roels et al., 2014). For instance, results from core flooding experiments, with porous media, have revealed bulk permeability reductions of around 15 - 86%, due to salt precipitation (Bacci et al., 2011; Kim et al., 2013; Tang et al., 2014), and these reductions have caused significant loss of injectivity in many of those cases (Wang et al., 2009; Golghanddashti et al., 2011).

While many reports of formation dry-out in porous media are available, studies about dry-out in *fractured* rocks in particular are scarce (Xu and Pruess, 2004; Borgia et al., 2012; Smith et al., 2013). Moreover, fluid flow in individual fractures usually exhibits channeling (Pyrak et al., 1987), which dominates fluid and solute transport within fractures (Brown et al., 1998) and eventually affects the dry-out process, as the salt precipitation patterns are intimately related to the flow. Channeling of flow is influenced by the fracture aperture field and roughness (Vogler et al., 2018). Therefore, it may not be possible to directly extrapolate results from formation dry-out investigations in porous media to fractured or fracture-dominated media. In this paper, we provide preliminary results of numerical simulations investigating the formation dry-out behavior in a brine-saturated single fracture during the injection of $scCO_2$, to better understand the physical mechanisms taking place under such conditions. The goals of this study are to (i) map aperture fields of naturally fractured granodiorite specimens via photogrammetric scans; (ii) numerically obtain aperture fields for different effective normal stresses; (iii) numerically model the two-phase, partially miscible flow of $scCO_2$ and brine

through a single granite fracture under typical subsurface geological conditions; (iv) investigate the macroscopic distribution (i.e. the progress of the dry-out zone, where salt precipitation occurs) of the precipitant after the injection of $scCO_2$; and (v) quantify the impact of the $scCO_2$ injection rate and the effective normal stress (on the fracture) on mineral precipitation patterns throughout the 2D open fracture space.

2. MODELLING FORMATION DRY-OUT PROCESSES

Different physical mechanisms can be identified at the macro scale during formation dry-out, in both porous and fracture-dominated media (Figure 1). First, once the $scCO_2$ is injected, it displaces the formation brine, away from the injection well, constituting two-phase flow that is governed by viscous forces. If the thickness of the reservoir formation is large enough, gravity override of injected CO_2 may also be relevant. Usually, the reservoir formation is heterogeneous, so that flow channels are expected to form during the displacement of the brine by the $scCO_2$. Second, counter-current imbibition of brine in the upstream direction might become relevant as the capillary pressure gradient increases, due to the decrease in brine saturation in the zone close to the $scCO_2$ injection well. This capillary-driven backflow can greatly increase the aqueous phase salinity, due to continuous replenishment of salt (Pruess and Mueller, 2009). Third, the continuous injection of dry $scCO_2$ vaporizes the remaining formation brine in the swept zone, which persistently increases the concentration of dissolved salt. When the salt concentration reaches the solubility limit, it precipitates out of the brine, thereby forming salt crystals in the fractured or porous medium. This salt precipitation inevitably reduces the porosity and likely decreases the related formation permeability, depending on the spatial distribution of the salt precipitation. The precipitated salt distribution apparently depends on the balance of dissolved salt diffusion and water evaporation processes, increasing the dissolved salt saturation, which can cause different drying regimes in porous media (Miri and Hellevang, 2016). All these processes should be included in numerical models that aim to reproduce formation dry-out processes.

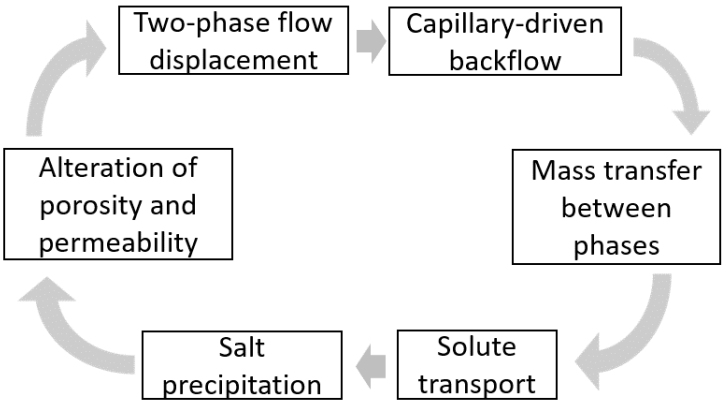

Figure 1: Potential salt precipitation processes during $scCO_2$ injection into reservoir brines.

In simplified models of salt precipitation in homogeneous porous media, under linear flow assumption, two main fronts are usually identified: a displacement front and a dry-out front, leading to three distinct zones (Figure 2) (Ghafoori et al., 2017; Nooraiepour et al., 2018). These two fronts travel from the injection well to the interior of the formation at different speeds and are expected to occur over different timescales (Miri and Hellevang, 2016). The displacement front is a typical immiscible front, which could be modelled using, for example, the Buckley-Leverett formulation (Buckley and Leverett, 1942). The saturation of the CO_2 phase at this front generally depends on the mobility ratio of brine/CO_2, thus low values are expected due to the significantly higher mobility of CO_2, compared to brine, under typical conditions of subsurface fluid flow. Behind this front, brine and $scCO_2$ flow simultaneously in the unsaturated zone and water constantly evaporates into the $scCO_2$ stream if $scCO_2$ has not been saturated with water yet. At a certain time, salt precipitation occurs near the injection well, so that the area, affected by this mineral precipitation, increases with time, as more dry $scCO_2$ is injected into the reservoir. A moving dry-out front is then developed, behind which only dry $scCO_2$ flows and all water is considered to have already evaporated. Hence, all solid salt precipitation is expected to occur behind the dry-out front, in the dried zone (Figure 2). This is also the zone, where the alteration of permeability can cause a loss of $scCO_2$ injectivity, especially due to its proximity to the injection well.

Based on this simplified model of two moving fronts, some analytical solutions have been proposed to investigate the process of formation dry-out in one-dimensional space (Pruess, 2009; Zeidouni et al., 2009). These solutions apply the standard fractional flow theory to study the displacement of brine by $scCO_2$ in a linear flow regime, but also use the same theory to approximate the advancement of the dry-out front, as if the dry-out front was also part of a two-phase displacement. Therefore, the problem is simplified to the analysis of the propagation of two different shock fronts (discontinuities in saturation and concentration), yet no change in phase is assumed. While these analyses assist in the understanding of the main mechanisms involved in salt precipitation during formation dry-out, they are too simplified to be scalable to full-scale reservoirs. For example, the analytical solution developed by Pruess (2009) is only valid for one-dimensional (1D) radial flow in a homogeneous and isotropic reservoir, and neglects interphase mass transfer and potential effects of capillary-driven backflow.

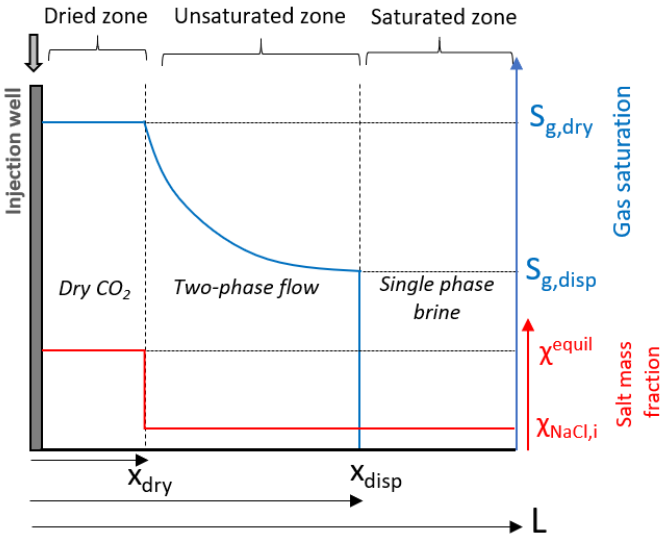

Figure 2: Zones developed during formation dry-out due to injection of CO_2 into brine-saturated, homogeneous reservoirs, where *L* is the distance from the injection wellbore; x_{disp} and x_{dry} are the positions of the displacement and the dry-out fronts, respectively; $S_{g,dry}$ and $S_{g,disp}$ are the saturations of CO_2 at the dry-out zone and at the displacement front, respectively; and χ_{equil} and $\chi_{NaCl,i}$ are the salt mass fractions at the solubility limit and under the initial reservoir condition, respectively.

In an attempt to study formation dry-out as reservoir scales and in more realistic scenarios, numerical simulators have been used, such as the general-purpose reservoir simulation code TOUGH2 (Xu and Pruess, 2004; Pruess, 2005; Bacci et al., 2013; Oh et al., 2013; Ghafoori et al., 2017). In such simulators, the salt is often considered as an additional chemical species (dissolved NaCl, halite), present only in the aqueous phase. Plus, the amount of precipitated salt is described in terms of solid saturation, which denotes the fraction of pore volume occupied by halite. Usually, reservoir simulators assume a local chemical equilibrium in the description of phase partitioning between CO_2 and brine, which might lead to significant errors in cases, where the evaporation rates are much smaller than the well injection velocities (Roels, 2015; Pan et al., 2016). In any case, in general the effect of the newly formed solid phase on *porosity* is automatically considered in these programs, as higher solid saturations lead to a reduced volume available for the fluid phases to flow through. In contrast, modelling the effect of salt precipitation on *permeability* is a more complex issue. Different approaches have been applied to coupling permeability to porosity in porous media, and amongst the most used ones are the cubic Kozeny-Carman grain model (Carman, 1929; Xu and Pruess, 2004) and the so-called tube in series model of Verma and Pruess (1988). With those approaches, the simulators attempt to capture $scCO_2$ injectivity losses, caused by salt precipitation. In field scale numerical models, however, fractures are often incorporated by using multi-continuum models, in which the fractures are simply represented as more permeable layers of a porous media (Oh et al., 2013) or treated as part of an effective continuum model (ECM) (Pruess et al., 1990). In such models, the heterogeneity of the fracture space is often neglected and no upscaling technique is typically applied to evaluate the effect of salt precipitation as a function of the fracture aperture distribution and heterogeneity.

3. MATERIAL AND METHODS

3.1 Fracture Characterization

In this study, we use naturally fractured granodiorite cores from the Deep Underground Geothermal (DUG) Lab at the Grimsel Test Site (GTS) in Switzerland (Figure 3a) (Tanaka et al., 2014; Vogler et al., 2016). One shear-fracture laboratory specimen (N18), with a diameter of 2.5 cm and length 3.0 cm, was chosen for aperture field characterization. Classification of the fracture followed criteria described by Vogler et al. (2017a).

The fracture surfaces of Specimen N18 were digitized with a photogrammetric ATOS Core 3D scanner. The calibration of the photogrammetry scanner was performed in such a way that the length deviation errors were between 0.009 and 0.027 mm, and the optimized calibration deviations were 0.014 ± 0.001 pixels (Vogler et al., 2016). Next, the fracture aperture field, under zero-stress condition, was determined after alignment of the two surfaces (Figure 3b), as described by Vogler et al. (2017a).

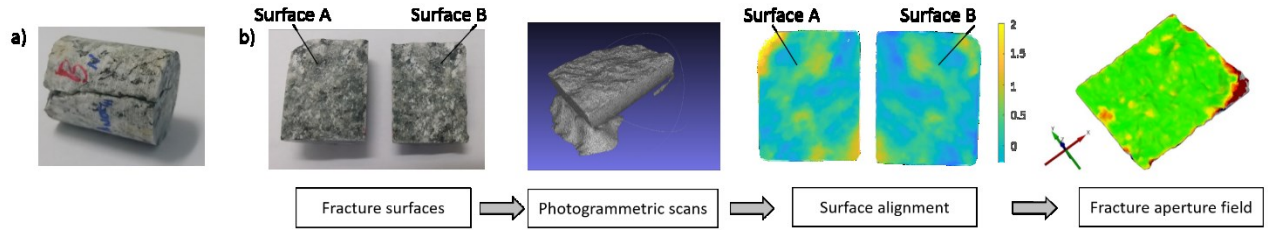

Figure 3: a) Specimen N18; b) Acquisition process of fracture aperture field via photogrammetry scanning.

Once the zero-stress fracture aperture field was obtained, the aperture distribution under 10 MPa effective normal stress (σ') was calculated, using a deterministic FFT-based contact mechanics code PyCo (Jacobs et al. 2017, Kling et al. 2018). Table 1 lists the mean and standard deviation of the aperture distributions under these two conditions (σ' = 0 MPa and 10 MPa). Figure 4 shows the aperture fields of Specimen N18 as well as the aperture distributions and the variation of the contact area and mean aperture with increasing stress, obtained from the contact model. Higher effective normal stress across the fracture leads to a smaller mean aperture and a larger contact area. These different aperture fields were then used to determine the aperture-based capillary pressures and to compose the meshes, used for the numerical simulations, as explained in the next sections.

Table 1: Aperture properties of Specimen N18 under different effective normal stress conditions.

Effective Normal Stress (MPa)	Mean aperture (μm)	Standard deviation (μm)
0	79.4	37.9
10	38.6	37.2

3.2 Numerical Model

3.2.1 Mesh and flow model

A MOOSE-based (Gaston et al., 2014) in-house application is used to model two-phase flow of brine displacement with $scCO_2$ injection into a fractured specimen, in order to study formation dry-out in a single fracture. The fracture is conceptualized as

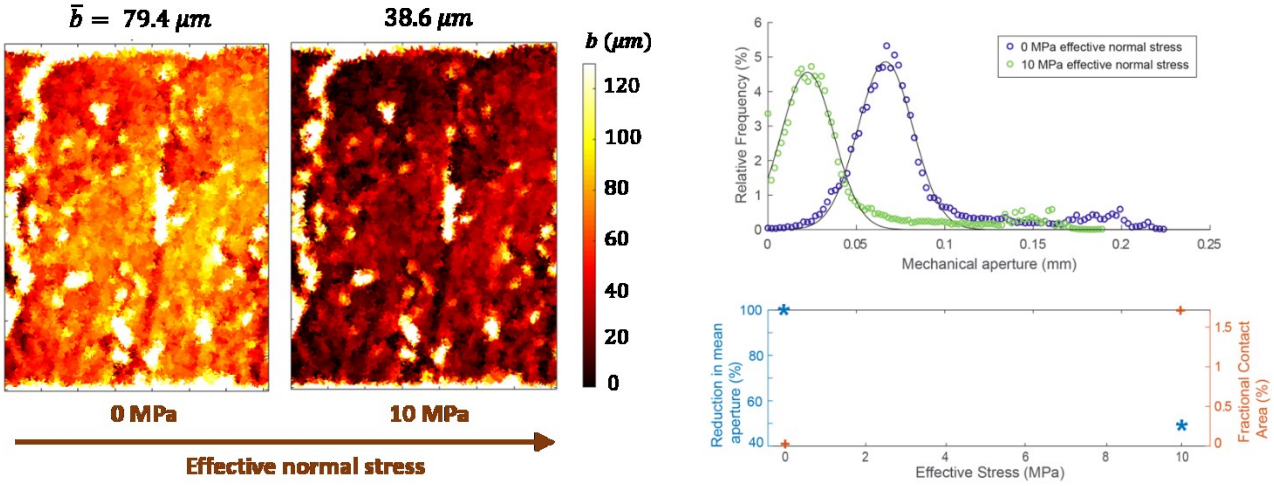

Figure 4: Aperture fields, probability distributions, and variations of mean aperture and contact area of Specimen N18 under increasing effective normal stress (0 MPa and 10 MPa), as obtained from the contact model application.

a two-dimensional (2D) aperture field with squared elements, and the aperture field is taken from the photogrammetry scans of the naturally fractured specimen after the normal stress was numerically applied (

Figure 5). In this preliminary phase of the study, in order to improve numerical stability, the system domain is set to 25 x 30 cm, which is 10 times larger than the rock specimen. Later, this 2D model is discretized into a mesh of 40 x 40 elements. The aperture of each element is evaluated using the parallel-plate assumption with a constant opening, and the fracture permeability is calculated using the so-called local cubic law, which is the classical model for fracture permeabilities (Wang et al., 1982; Zimmerman and Yeo, 2000). Studies have shown that the local cubic law is plausible, when the fluid flow within the fracture is laminar and the Reynolds number (Re) for flow in a single fracture (Equation 1) is less than 1 (Brush and Thomson, 2003),

$$Re = \frac{\rho \cdot l_v \cdot U_i}{\mu} = \frac{\rho \cdot \bar{b} \cdot Q}{\mu \cdot \bar{b} \cdot w} = \frac{\rho \cdot Q}{\mu \cdot w} \quad (1)$$

where ρ [kg m^{-3}] is the density of the fluid, l_v [m] is the characteristic length of the viscous forces, U_i [m s^{-1}] is the characteristic velocity for inertial forces, μ [Pa s] is the dynamic viscosity of the fluid, Q [m^3 s^{-1}] is the volumetric flow rate, w [m] is the width of the specimen fracture, and $\bar{b}$ [m] is the mean aperture of the element. In this study, the Reynolds number was smaller than 1 for the base-case simulation, permitting the use of the cubic law and consequently Darcy's law to numerically model fluid flow.

The initial conditions are set to 90°C for the temperature and 15 MPa for the pore pressure (

Figure 5), which corresponds to the conditions of a cold and shallow reservoir (Nordbotten et al., 2005). This pressure is kept constant at the outflow boundary of the numerical model. An inlet constant injection flux of 5.6×10^{-7} kg/s mimics the conditions of planned future laboratory experiments. This injection flux corresponds to an average linear velocity of $scCO_2$ inside the fracture space of approximately 10^{-2} m/s, which is in the range of relatively fast flow conditions (Molins et al., 2017) and is appropriate for modelling near-well conditions. Heat transport is not modelled, hence the temperature remains constant over time. No-flow Neumann boundary conditions are imposed at the left and right domain boundaries (

Figure 5). Additionally, the interfacial tension between brine and $scCO_2$ is considered constant at 30 mN/m (Pereira et al., 2017) and the contact angle is considered to be zero, i.e., complete wetting is assumed.

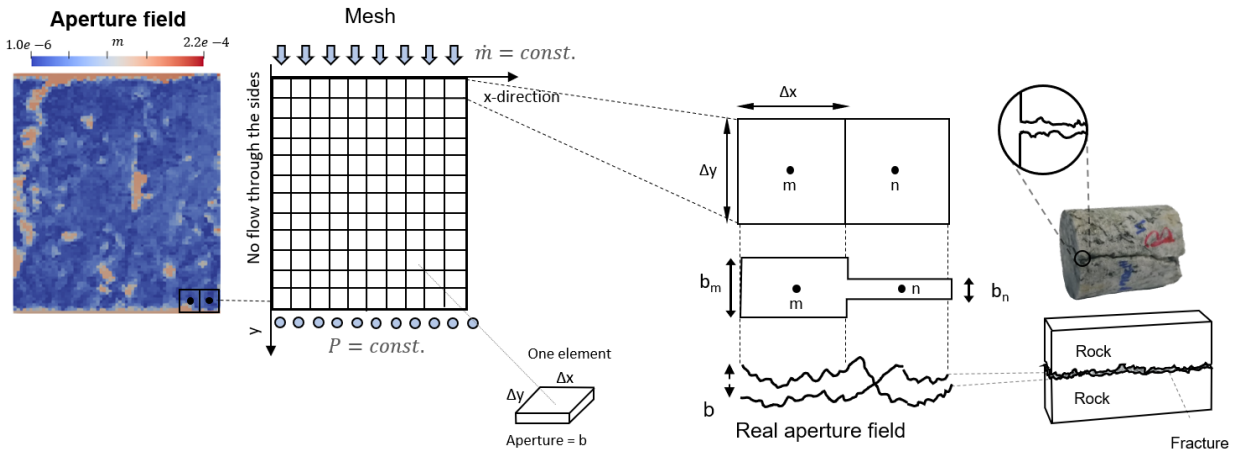

Figure 5: Model of the fracture aperture field, employed during numerical simulations. Shown is the fracture aperture field at 10 MPa of effective normal stress (left), an illustration of the 2D mesh used in the fracture plane (center left), and an illustration of how two neighboring mesh cells are modeled during the 2D approach (right).

3.2.2 Two-phase flow properties

The utilized MOOSE PorousFlow module provides access to high precision equations of state for both brine and $scCO_2$, including the mutual solubility of $scCO_2$ into the liquid brine and water into the $scCO_2$-rich gas phase. For temperatures below 100°C, the mass fractions of $scCO_2$ in the liquid phase and H_2O in the gas phase are calculated using the accurate fugacity-based formulation, presented by Spycher et al. (2003) and Spycher et al. (2005), which is similar to the formulation provided in the ECO2N module of TOUGH2 (Pruess and Spycher, 2007). Dissolution of $scCO_2$ into the brine and evaporation of water vapor into the $scCO_2$ phase are assumed to happen instantaneously, which means that the phases are in instantaneous chemical equilibrium and no reaction kinetics are modelled.

For the relative permeability of brine and $scCO_2$, the Corey correlation (Corey, 1954) is used, with parameters n = 2 and residual water saturation of 10%. To model the capillary pressure, however, capabilities of the MOOSE framework were extended by implementing the Young-Laplace equation (Equation 2) in an in-house application (Grimm Lima et al., 2019).

$$P_c = \frac{2\gamma_{CO_2-brine}cos\theta}{b} \quad (2)$$

where $\gamma_{CO2\text{-}brine}$ [N m^{-1}] is the interfacial tension, θ is the contact angle, and b [m] is the void aperture.

3.2.3 Chemical system

Table 2 describes the chemical system studied in our numerical model. Halite (NaCl) is considered the only salt present in the brine, which is a good approximation as NaCl is the most abundant salt in formation brines (Xu and Pruess, 2004). The components H_2O and $scCO_2$ can exist in both the aqueous phase (also called liquid phase) and the supercritical phase (also called gaseous phase), but NaCl can only exist in the aqueous phase. This approach is similar to the ones applied in commercial simulators, such as TOUGH2 (Pruess, 2005). On top of these traditional approaches, a less frequently used concept is adopted for the solid phase in the present study. Instead of forming a solid phase, the amount of salt precipitation is calculated separately, based on the amount of vaporization (Zeidouni et al., 2009), and this amount is used to promote *fracture aperture alteration*, as described in Section 3.2.4. The chemical system has therefore only two phases: liquid and gaseous, unlike other simulators that rely on three phases (liquid, gas, and solid) to study formation dry-out (Xu and Pruess, 2004; Giorgis et al., 2007; Bacci et al., 2013; Roels, 2015). Eventual geochemical reactions between the fluids and the granite are not modelled, as fluid-rock reactions are expected to be slow and therefore insignificant for the timescales considered in our simulations. Consequently, in this study, the treatment of solid precipitation during injection-induced formation dry-out focuses exclusively on the precipitation of dissolved salt (NaCl), while the rock minerals are assumed to be non-reactive.

Table 2: Phases and chemical species.

Phase	Chemical Species
Aqueous phase	$H_2O(aq)$, $H^+(aq)$, $OH^-(aq)$, $HCO_3^-(aq)$, $CO_3^{2-}(aq)$, $CO_2(aq)$, $Na^+(aq)$, $Cl^-(aq)$, NaCl(aq)
Gaseous (supercritical) phase	$H_2O(g)$, $CO_2(g)$

3.2.4 Aperture alteration due to halite precipitation

In our numerical model, salt (NaCl) precipitation occurs whenever the halite concentration in the brine reaches the solubility limit under the temperature and pressure conditions of the fluid. The salt mass fraction in the aqueous phase (χ_{nacl}) is therefore considered as a non-linear variable, in a system of two components (water + dissolved NaCl salt), which is similar to the approach of ECO2N module of TOUGH2 (Pruess, 2005). Diffusion and advection of the salt component within the aqueous phase is already implemented in the PorousFlow module of the MOOSE framework. However, so far, the chemical reactions, available in the PorousFlow module, are only suitable for fully-saturated aqueous geochemical systems, not for multi-phase physics. Thus, in our

case, since the processes involved in formation dry-out are inevitably multi-phase, a new numerical modelling strategy needed to be implemented. Hence, we coded halite precipitation as an intermediate step that reduces the fracture aperture, which, in turn, changes the porosity and the permeability of the system as well as the capillary pressure, as these properties are ultimately calculated based on the value of the aperture variable in our model.

Therefore, the fracture aperture variable, *b*, is set to evolve according to Equation 3:

$$\dot{b} = -bS_{liquid}R, \tag{3}$$

where S_{liquid} [-] is the saturation of the aqueous phase and R [-] is the precipitation rate, which can be calculated according to Equation 4:

$$R = r\left(\chi_{NaCl} - \chi^{equilibrium}\right), \tag{4}$$

where r [-] is the mineral precipitation rate coefficient and $\chi^{equilibrium}$ [kg kg^{-1}] is the solubility limit of the salt under a given pressure and temperature condition (Roels, 2015).

Analogously to TOUGH2 (Pan et al., 2012), the possibility of the start of mineral precipitation is evaluated by comparing χ_{nacl} with $\chi^{equilibrium}$. If $\chi_{nacl} < \chi^{equilibrium}$, no mineral precipitation occurs, whereas for $\chi_{nacl} > \chi^{equilibrium}$ mineral precipitation commences. In the latter case, once precipitation takes place, χ_{nacl} is set to equal $\chi^{equilibrium}$ and the aperture alteration, due to mineral precipitation, is computed. No solid phase is formed, but the fracture aperture value of the 2D-squared element is updated, as a result of the salt mass fraction having reached (and exceeded) the solubility limit (Equations 3 and 4). A new fracture void aperture leads to a new porosity and permeability, which eventually alters the fluid flow paths and fluid velocity fields in the single fracture model. In order to account for this clogging process, the precipitated salt is assumed to become uniform layers of thickness τ, deposited along the top and bottom walls of the element (Figure 6) (Giorgis et al., 2007), thereby resulting in aperture reductions proportional to the precipitated mineral volume.

Equation 3 will be implemented, employing a lagged approach:

$$b = b_{old} - dt \cdot b_{old}S_{liquid}r\left(\chi_{NaCl} - \chi^{equilibrium}\right) \tag{5}$$

where b_{old} is the value of the fracture void aperture before mineral precipitation occurred and *dt* is a simulation time step. This equation is subject to the constraint $b \geq 0$.

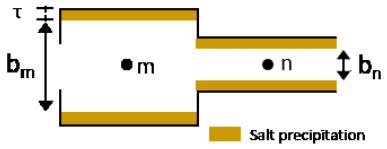

Figure 6: Clogging model of uniform layers of salt precipitation along the top and bottom of the fracture walls.

3.3 Simulation Setup

As described in the last section, the complete numerical model will include precipitation of halite and alteration of the fracture aperture, derived from the salt precipitates. While this part of the numerical code is being finalized, preliminary simulations were performed to evaluate the evolution of the salt concentration in the aqueous phase, after $scCO_2$ injection. In this intermediate step of the study, no solubility limit is established for the salt in the aqueous phase, therefore the salt mass fraction can virtually reach 100% due to water evaporation. This is physically inaccurate, as the salt precipitation is expected to occur as soon as the salt concentration reaches the solubility limit, at which point the salt mass fraction should stay at the solubility limit value and not go beyond it. However, results from simulations with this inaccuracy can still be useful for sensitivity analysis and for comparisons with other features not directly impacted by the salt concentration.

The base case simulation model is set for aperture distributions under 10 MPa of effective normal stress, a temperature of 90 °C, initial brine salinity of 20%, and a Péclet number, *Pe*, of 0.8 (Table 3). The Péclet number for flow in a fracture can be calculated by: using Equation 6 (Peysson et al., 2014):

$$Pe = \frac{Q \cdot \beta \cdot L}{w \cdot \bar{b} \cdot D \cdot \varphi \cdot \rho_w} \tag{6}$$

where the porosity, φ, is assumed to be equal to 1, Q is the injection flow rate [m^3 s^{-1}], L [m] is the sample length, w [m] is the fracture width, ρ_w [kg m^{-3}] is the water density, β [kg m^{-3}] is the water vapor concentration (β = 0.4 kg/m^3 at 90°C (Peysson et al., 2014)), and D [m^2 s^{-1}] is the diffusion coefficient ($D = 10^{-10}$ m^2/s for salt water (Peysson et al., 2014)), considering the fracture porosity equals 1.

The influence of the fluid flow rate is then investigated with different Péclet numbers: 0.08, 0.8, and 8, obtained by varying Q. Next, the influence of the effective normal stress across the fracture is studied by running comparative simulations for a fracture aperture distribution under zero effective normal stress. Finally, the mean aperture widths of the fractures under 0 MPa and 10 MPa serve as inputs to model two cases of uniform aperture widths, which are eventually compared to the heterogeneous cases to evaluate the impact of the aperture distribution on the two-phase flow. The different values of the parameters tested are listed in Table 4.

Table 3: The primary input parameters used in the simulation of the evolution of salt concentration due to $scCO_2$ injection into a saline aquifer.

Parameter	Value	Parameter	Value
Temperature (°C)	90	Initial salinity (%)	20
Péclet number	0.8	S_{wirr} (%)	10
Aperture distribution	Under 10 MPa*	Pore pressure (MPa)	15

**Effective normal stress (σ')*

Table 4: Different values of the parameters used in the sensitivity analysis.

Parameter	Base case value	Change 1	Change 2
Péclet number	0.8	0.08	8
Aperture distribution	Under 10 MPa*	Under 0 MPa*	Uniform fields

**Effective normal stress (σ')*

4. RESULTS AND DISCUSSION

4.1 Base Case

For the base case simulation (Table 3), the progress of the saturation of $scCO_2$ (S_{scCO_2}) over time is shown in Figure 7a. In addition to the 2D spatial maps, the values of $scCO_2$ saturation are averaged across the fracture width and approximate linear profiles are plotted across the fluid flow direction (Figure 7b), so that the results can be compared with 1D analytical solutions. From the analysis of the linear profiles of $scCO_2$ saturation during the early stages, the value of $S_{scCO_2}^{front}$ = 10% was taken to represent the saturation of $scCO_2$ at the displacement front. This threshold value is then highlighted as a white color contour in Figure 7a. Besides the $scCO_2$ saturation, the linear profiles of the salt mass fractions (χ_{NaCl}) for different times are also shown in Figure 7b, where any value of χ_{NaCl} higher than the halite solubility limit in water (χ^{equil}) was corrected and leveled to χ^{equil}, for the sake of graphical representation. Under the conditions of the base case, the solubility of halite in water is 384.7 g/L (Lide, 2005), which corresponds to a limit of 27.8% salt mass fraction. To depict the progress of the potential dry-out front, a salt solubility limit curve (χ_{NaCl} = 27.8%) is drawn in black color in Figure 7a, on top of the $scCO_2$ saturation map.

The $scCO_2$ displacement front propagates quickly (Figure 7), reaching the fluid production end in around 5 s. The heterogeneity of the fracture void space, under 10 MPa of effective normal stress, yields channeling, which is expected for fluid flow in fractures (Brown et al., 1998). This channeling effect contributes to the low $scCO_2$ saturation (~10%) at the displacement front, as low spatial sweep efficiency is promoted. The high mobility ratio of CO_2 to brine yields low displacement efficiencies, which adds to the low sweep efficiency and converges to an overall low flooding efficiency. In any case, due to the small size of the mesh, the fracture is completely swept by $scCO_2$ in less than 5 minutes. In contrast to the rapid propagation of the displacement front, the behavior of the dry-out front is yet different. While the displacement front appears immediately after the start of the injection, and reaches the production border in 5 s, the dry-out front appears only after 4 minutes of injection and continues to propagate at a much slower speed. These results are expected, as the physical mechanisms that define the progress of the dry-out front act at different time scales than the ones that influence the progress of the displacement front (Miri and Roland, 2016). This time scale separation of the progress of the two fronts has also been identified in previous studies both experimentally and numerically (Pruess and Müller, 2009; Peysson, 2012; Nooraiepour et al., 2018).

4.2 Sensitivity Analysis

The first sensitivity analysis is performed by varying the Péclet number of the simulations, yielding in different results (Figure 8). Considering a fixed point in time (60 s after $scCO_2$ injection), the salt dry-out front naturally progresses faster in the case of higher injection rate (Pe = 8), while the salt dry-out front has not formed yet for the lower injection rate (Pe = 0.08) (Figure 8a,b). However, a more conclusive evaluation can only be performed when the three cases are compared under the condition of the same *total $scCO_2$ mass injected*, not at the same time instant (Figure 8c,d). To achieve this condition, each case is depicted at a different time: 6000 s, 600 s and 60 s, for the cases of Pe = 0.08, 0.8 and 8, respectively. Under this condition, while for the cases of Pe = 0.8 and Pe = 8 the dry-out fronts are very similar to each other, the dry-out front in the case of Pe = 0.08 is more uniform and retracted. This uniformity suggests that the drying regime occurring in the case of the lowest Péclet number (Pe = 0.08) is different than the drying regime of the two other cases (Pe = 0.8 and Pe = 8). According to the classification proposed by Miri and Roland (2016) for porous media, the case of Pe = 0.08 presents characteristics of a *diffusive regime,* while the other cases can be considered *evaporative regimes.* In diffusive regimes, the evaporation rate is very low and the diffusion of salt can occur efficiently, resulting in a rather homogeneous distribution of salt throughout the medium. In contrast, evaporative regimes tend to produce dry-out fronts that advance at a constant velocity from the fluid inlet toward the outlet, as they immediately evaporate the trapped brine along the non-homogeneous migration path (shown in Figure 8 for the two cases of high Péclet numbers). The impact of injection rate on controlling the salt precipitation process has also been observed by other researchers (Giorgis et al., 2007; Ott et al., 2011; Oh et al., 2013, Jeddizahed and Rostami, 2016).

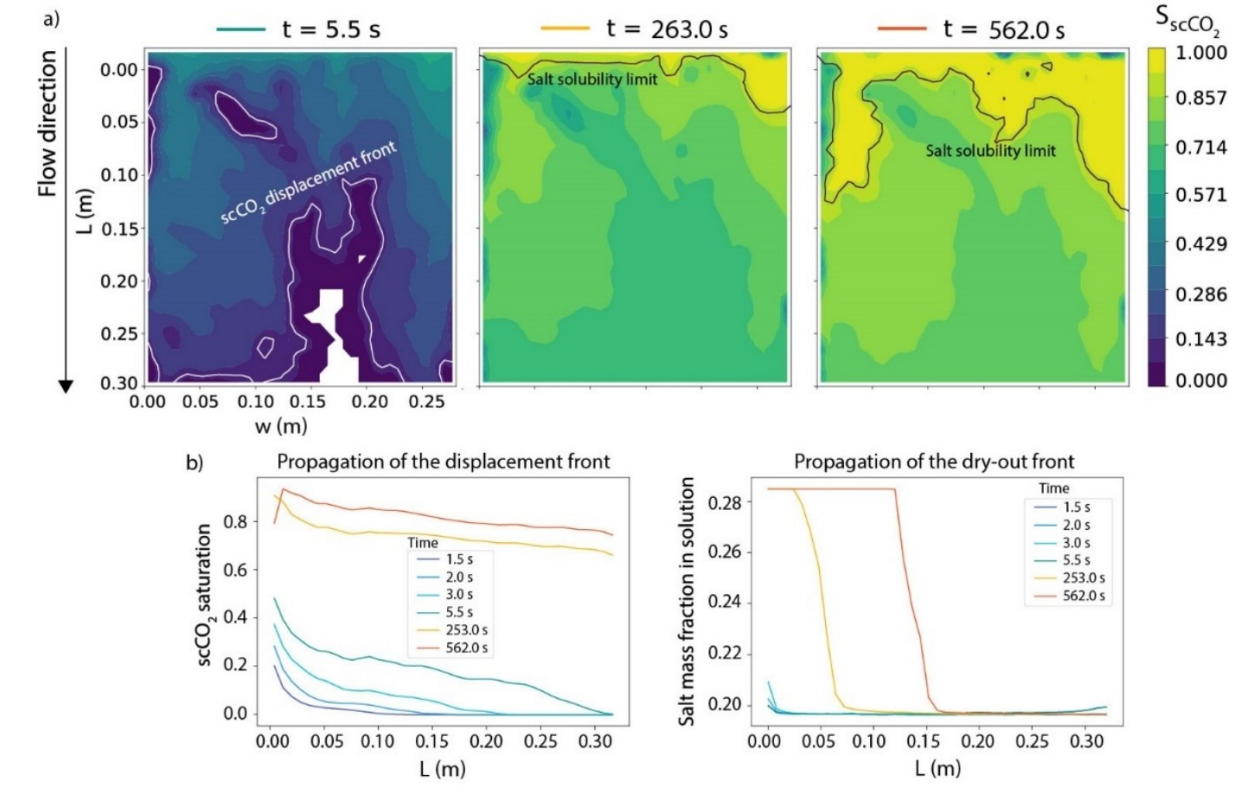

Figure 7: Results of the base case numerical simulation on $scCO_2$ injection into Specimen N18: a) saturation by the $scCO_2$ phase at an early stage and at two later stages after start of injection. The displacement front is shown as a white contour line. The dry-out front is sketched as a black contour line. Constant $scCO_2$ mass injection occurs at the top and no-flow boundary conditions are set to the sides; b) averaged values of $scCO_2$ saturation (left panel) and salt mass fraction in the aqueous solution (right panel) across the flow direction, during early stages (blue and green colors) and later stages (yellow and orange colors), after the start of the $scCO_2$ injection.

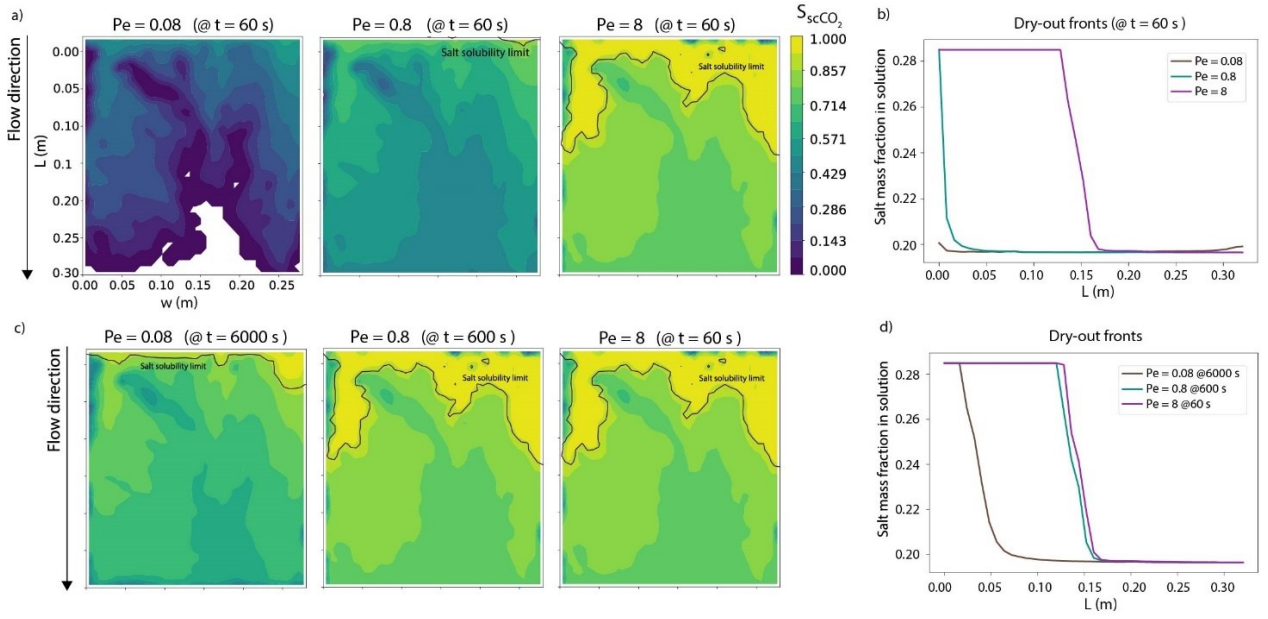

Figure 8: Numerical simulation results for $scCO_2$ injection into Specimen N18: dry-out front in different cases of Péclet numbers, at time 60 s (a, b) and at different times for each Péclet number (0.08, 0.8, and 8): 6000 s, 600 s, and 60 s, respectively (c, d).

The to-date last sensitivity analysis is performed by varying the fracture aperture fields, in order to investigate the impact of the effective normal stress across the fracture and the fracture heterogeneity on the progress of the dry-out front. Figure 9 shows the results of the $scCO_2$ saturation distribution 650 s after the start of $scCO_2$ injection for four different fracture aperture fields: aperture fields under $\sigma' = 0$ MPa and $\sigma' = 10$ MPa (Figure 9a), and two uniform aperture fields with apertures of 79.4 μm and 38.6 μm (Figure 9b), which correspond to the mean aperture of the heterogeneous fields (Table 1). The dry-out front propagates more uniformly in the aperture field under zero effective normal stress, as there are only few regions with low permeabilities in the fracture plane (Figure 4). For the case of higher effective normal stresses, as previously observed by Grimm Lima et al. (2019), the

aperture distribution becomes more heterogeneous and promotes the channeling of fluid flow, which affects the progress of the dry-out front. Progress of the dry-out fronts in the uniform aperture fields (Figure 9b) is slower than their corresponding heterogeneous cases (Figure 9c). This delay is not significant when no effective normal stress is applied, as even the corresponding heterogeneous aperture field does not result in strong fluid flow channeling. However, the delay is substantial for the aperture field under 10 MPa effective normal stress. This divergence suggests that approximating the whole fracture void space by two parallel plates, with a constant aperture, should be done with caution, as it can lead to errors if the fracture aperture is heterogeneous. This holds especially true if the goal is to numerically reproduce laboratory experiments, where small rock specimens are usually used. For field-scale simulations, however, other uncertainties involved are usually larger, including insufficient knowledge of a reservoir's geologic structure and heterogeneities in reservoir properties. Therefore, in reservoir scale, the uncertainties associated to upscaling techniques and geometry

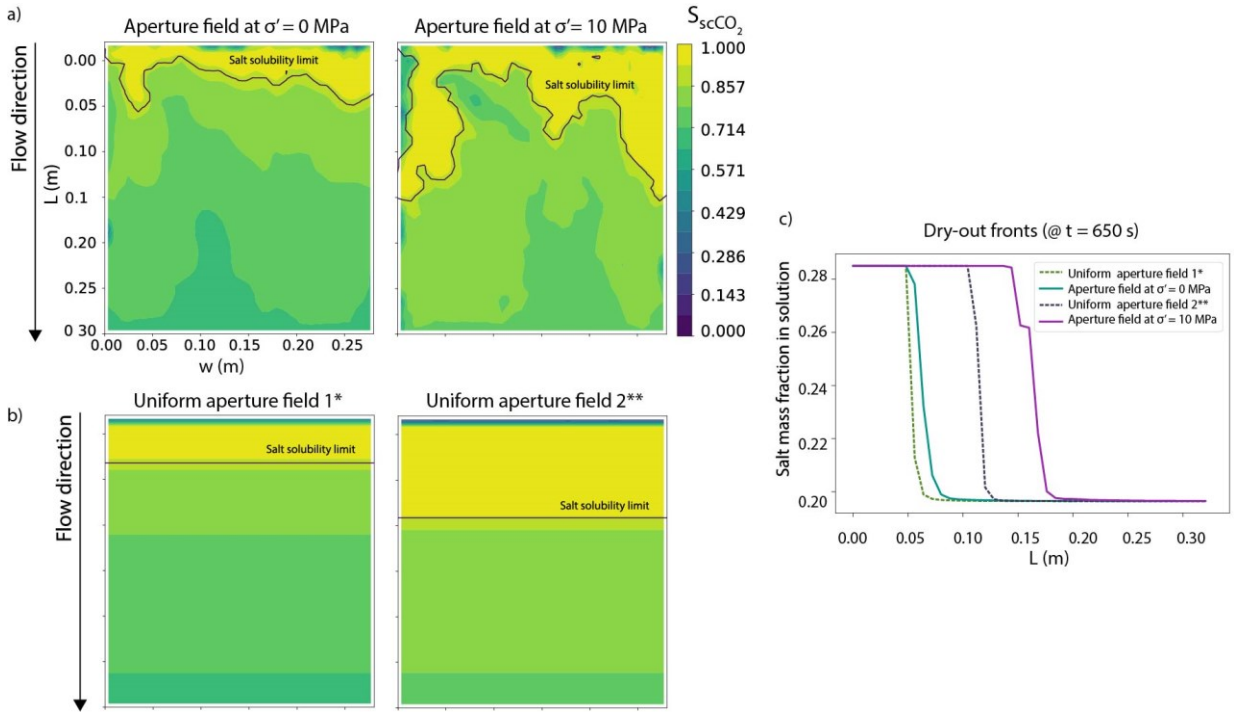

**The uniform aperture field 1 was set with the same mean void aperture as the one of the aperture field under σ' = 0 MPa.*
***The uniform aperture field 2 was set with the same mean void aperture as the one of the aperture field under σ' = 10 MPa.*

Figure 9: Results of numerical simulations on $scCO_2$ injection into Specimen N18: dry-out front in different aperture fields and cases of effective normal stress, σ', all at 650 s since $scCO_2$ injection started, and with a Péclet number of 0.8 (base case).

5. CONCLUSIONS

A numerical model is presented to investigate the injection of supercritical CO_2 ($scCO_2$) into single brine-saturated fractures under subsurface geological conditions of a cold and shallow reservoir. The model aims at representing two-phase viscous displacement, capillary-driven backflow, multicomponent phase equilibria, mineral precipitation, and consequential changes in porosity and permeability, with the focus on the phenomenon of $scCO_2$ injection-driven formation dry-out. The simulations are conducted on naturally fractured specimens which are scanned via photogrammetry and the stress-dependent aperture fields are numerically obtained using a contact mechanics model.

The results of the simulations show that the development of two distinct moving fronts (the displacement and the dry-out fronts), identified over different time scales. Moreover, the injection rate is found to directly influence the drying regime of the formation dry-out and the salt precipitation distribution, as the balance between diffusion and evaporation rates varies with the change of the Péclet number. Finally, our numerical simulations reveal a high impact of the fracture aperture field heterogeneity and the aperture field variation, which depend on the effective normal stress conditions, on the dry-out front propagation. More specifically, when simulating laboratory experiments, the fracture aperture field heterogeneity should be well characterized in a numerical model, as the flow results are greatly influenced by this heterogeneity.

In future work, investigating the impact of mineral precipitation on fracture aperture will be crucial to properly assess the decrease of fluid injectivity during formation dry-out. A numerical model that can represent properly the interplay between the different physical mechanisms assist in an improved interpretation of results from laboratory experiments and facilitates upscaling efforts from the rock core to the field or reservoir scale. This work has implications for several geoscience applications, including enhanced geothermal systems using $scCO_2$ and geological $scCO_2$ sequestration in fracture-dominated reservoirs. During the long-term operation of such geologic systems, the potential effects of salt precipitation should be a major concern, considering the risk of a significant decrease in reservoir permeability as well as impairment of $scCO_2$ injectivity.

ACKNOWLEDGEMENTS

The authors want to thank the chair of Geosensors and Engineering Geodesy at ETH Zurich and especially Robert Presl for their support with the photogrammetry scanner. The authors want to thank Andrew Wilkins for his support with the formulation of the numerical problem and with the MOOSE PorousFlow module in general. This work was supported by ETH Research Grant ETH-02 16-2. The Werner Siemens Foundation (Werner Siemens-Stiftung) is further thanked for its support of the Geothermal Energy and Geofluids Group at ETH Zurich.

REFERENCES

André, L., Peysson, Y., and Azaroual, M.: Well injectivity during CO_2 storage operations in deep saline aquifers – Part 2: Numerical simulations of drying, salt deposit mechanisms and role of capillary forces., *International Journal of Greenhouse Gas Control*, **22**, (2014), 301—312.

Bacci, G., Korre, A., and Durucan, S.: Experimental investigation into salt precipitation during CO_2 injection in saline aquifers. *Energy Procedia*, **4**, (2011), 4450–4456.

Bacci, G.; Durucan, S., and Korre, A. Experimental and Numerical Study of the Effects of Halite Scaling on Injectivity and Seal Performance During CO_2 Injection in Saline Aquifers, *Energy Procedia*, **37**, (2013), 3275-3282.

Baumann, G., Henninges, J., and De Lucia, M.: Monitoring of saturation changes and salt precipitation during CO_2 injection using pulsed neutron-gamma logging at the Ketzin pilot site*., Int. J. Greenh. Gas Control*, 28, (2014), 134–146.

Borgia, A., Pruess, K. , Kneafsey, T. J. , Oldenburg, C. M., and Pan, L.: Simulation of CO_2-EGS in a fractured reservoir with salt precipitation, *Energy Procedia*, **37**, (2013), 6617-6624.

Brown, S., Caprihan, A., and Hardy, R.: Experimental observation of fluid flow channels in a single fracture. *Journal of Geophysical Research: Solid Earth*, **103,** (1998), 5125–5132.

Brown, D. W.: A hot dry rock geothermal energy concept utilizing supercritical CO_2 instead of water., *Proceedings,* 25th Workshop on Geothermal Reservoir Engineering, Stanford University, Stanford, CA (2000).

Brush, D. J. and Thomson, N.: Fluid flow in synthetic rough-walled fractures: Navier-Stokes, Stokes, and local cubic law simulations, *Water Resources Research*, **39**, (2003).

Buckley, S. E. and Leverett, M.C. : Mechanism of fluid displacement in sands, *Trans. Am. Inst. Min. Metall. Eng.,* **146**, (1942), 107– 116.

Carman, P. C.: Permeability of saturated sand, soil and clay, *J. Agr. Sci.,* **29**, (1939), 263–273.

Corey., A. T.: The interrelation between gas and oil relative permeabilities. *Prod. Month.*, **19**, (1954), 38–41.

Ghafoori, M.; Tabatabaei-Nejad, S. A., and Khodapanah,E. Modeling rock-fluid interactions due to CO_2 injection into sandstone and carbonate aquifer considering salt precipitation and chemical reactions, *Journal of Natural Gas Science and Engineering*, **37**, (2017), 523-538.

Gaston, D. R.; Peterson, J. W.; Permann, C. J.; Andrs, D.; Slaughter, A. E., and Miller, J. M.: Continuous integration for concurrent computational framework and application development. *Journal of Open Research Software*, **2**, (2014), 1–6.

Giorgis, T., Carpita, M., and Battistelli, A.: 2D modeling of salt precipitation during the injection of dry CO_2 in a depleted gas reservoir., *Environmental Geology*, **48**, (2007), 1816-1826.

Golghanddashti, H., Saadat, M., Abbasi, S., and Shahrabadi, A.: Experimental Investigation of Salt Precipitation during Gas Injection into a Depleted Gas Reservoir, *Proceedings,* International Petroleum Technology Conference, 15–17 November, Bangkok, IPTC, Thailand, (2011).

Golghanddashti, H., Saadat, M., Abbasi, S., and Shahrabadi, A.: Experimental investigation of water vaporization and its induced formation damage associated with underground gas storage. *Journal of Porous Media*, **16**, (2013), 89–96.

Grimm Lima, M. M.; Schädle, P.; Vogler, D.; Saar, M. O., and Kong, X.-Z.: Impact of Effective Normal Stress on Capillary Pressure in a Single Natural Fracture, *Proceedings,* European Geothermal Congress 2019, 11-14 June, The Hague, The Netherlands, (2019).

Hansen, O., Gilding, D., Nazarian, B., Osdal, B., Ringrose, P., Kristoffersen, J.-B.,Eiken, O., and Hansen, H.: Snøhvit: the history of injecting and storing 1 Mt CO_2 in the fluvial Tubåen Fm. *Energy Procedia*, **37**, (2013), 3565–3573.

Jacobs, T., Junge, T., and Pastewka, L. Quantitative characterization of surface topography using spectral analysis. *Surf. Topogr. Metrol. Prop.,* **5**, (2017).

Jeddizahed, J., Rostami, B.: Experimental investigation of injectivity alteration due to salt precipitation during CO_2 sequestration in saline aquifers, *Advances in Water Resources*, **96**, (2016), 23-33.

Kim, M., Sell, A., and Sinton, D.: Aquifer-on-a-chip: understanding pore-scale salt precipitation dynamics during CO_2 sequestration. *Lab Chip*, **13**, (2013), 2508–2518.

Kleinitz, W., Koehler, M., and Dietzsch, G.: The precipitation of salt in gas producing wells., *Proceedings*, SPE European Formation Damage Conference, The Hague, Netherlands, (2001).

Kling, T., Vogler, D., Pastewka, L., Amann, F., and Blum, P. Numerical Simulations and Validation of Contact Mechanics in a Granodiorite Fracture, *Rock Mechanics and Rock Engineering*, **51**, (2018), 2805-2824.

Lide, D. R., ed. CRC Handbook of Chemistry and Physics, CRC Press, Boca Raton, FL, (2005).

Maxwell, D. and Young, K.: Concept, Design and Implementation of a Halite Scale Mitigation Completion in a Gas Well, *Proceedings,* SPE International Oilfield Scale Conference and Exhibition, 14-15 May, Aberdeen, Scotland, (2014).

Miri, R. and Hellevang, H.: Salt precipitation during CO_2 storage—A review, *International Journal of Greenhouse Gas Control*, **51**, (2016), 136-147.

Molins, S., Trebotich, D., Miller, G. H., and Steefel, C. I.: Mineralogical and transport controls on the evolution of porous media texture using direct numerical simulation. Water Resour. Res., **53** (5), (2017) 3645−3661.

Muller, N., Qi, R., Mackie, E., Pruess, K., and Blunt, M. J.: CO_2 injection impairment due to halite precipitation. *Energy Procedia*, **1**, (2009), 3507–3514.

Nooraiepour, M., Fazeli, H., Miri, R., and Hellevang, H.: Effect of CO_2 Phase States and Flow Rate on Salt Precipitation in Shale Caprocks - A Microfluidic Study, *Environmental Science & Technology*, **52**, (2018), 6050-6060.

Nordbotten, J. M., Celia, M. A., Bachu, S.: Injection and Storage of CO_2 in Deep Saline Aquifers: Analytical Solution for CO_2 Plume Evolution During Injection. *Transport in Porous Media*, **58**, (2005), 339-360.

Oh, J.; Kim, K.-Y.; Han, W. S.; Kim, T.; Kim, J.-C., and Park, E.: Experimental and numerical study on supercritical CO_2/brine transport in a fractured rock: Implications of mass transfer, capillary pressure and storage capacity, *Advances in Water Resources*, **62**, Part C, (2013), 442-453.

Ott, H., de Kloe, K., Marcelis, F., and Makurat, A.: Injection of supercritical CO_2 in brine saturated sandstone: Pattern formation during salt precipitation. *Energy Procedia*, **4**, (2011), 4426–4432.

Pan, L.; Spycher, N.; Doughty, C., and Pruess, K.: ECO2N V2.0: A TOUGH2 fluid property module for modeling CO_2 -H_2O-NaCl systems to elevated temperatures of up to 300°C., *Original Research Article: Greenhouse Gases: Science and Technology*, **7**, 2, (2016), 313-327.

Pereira, L. M., Chapoy, A., Burgass, R., and Tohidi, B. Interfacial tension of CO_2+brine systems: Experiments and predictive modelling., *Adv. Water Resour.,* **103**, (2017), 64-75.

Peysson, Y.: Permeability alteration induced by drying of brines in porous media. *The European Physical Journal Applied Physics*, **60**, (2012).

Peysson, Y., André, L., Azaroual, M.: Well injectivity during CO2 storage operations in deep saline aquifers—Part 1: Experimental investigation of drying effects, salt precipitation and capillary forces, *International Journal of Greenhouse Gas Control*, **22**, (2014), 291-300.

Pruess, K.; Wang, J. S. Y., and Tsang, Y. W.: On thermohydrological conditions near high-level nuclear wastes emplaced in partially saturated fractured tuff, Part 2, Effective continuum approximation, *Water Resources Research*, 26, (1990), 1249–1261.

Pruess, K. and Garcia, J.. Multiphase flow dynamics during CO_2 injection into saline aquifers. *Environmental Geology*, **42**, (2002), 282-295.

Pruess, K.: ECO2N: A TOUGH2 Fluid Property Module for Mixtures of Water, NaCl, and CO_2: *Lawrence Berkeley National Laboratory,* (2005).

Pruess, K.: Enhanced Geothermal Systems (EGS) Using CO_2 as Working Fluid: A Novel Approach for Generating Renewable Energy with Simultaneous Sequestration of Carbon, *Geothermics*, **35**, (2006), 351-367.

Pruess, K. and Spycher, N.: ECO2N – A fluid property module for the TOUGH2 code for studies of CO_2 storage in saline aquifers, *Energy Conversion and Management*, **48**, 6, (2007), 1761-1767.

Pruess, K. and Mueller, N.: Formation dry-out from CO_2 injection into saline aquifers: 1. Effects of solids precipitation and their mitigation. *Water Resources Research*, **45**, (2009) A426–A426.

Pruess, K.: Formation dry-out from CO_2 injection into saline aquifers: 2. Analytical model for salt precipitation., *Water Resources Research*, **45**, (2009).

Pyrak-Nolte, L. J., Myer, L. R., Cook, N. G. W., and Witherspoon, P. A.: Hydraulic and mechanical properties of natural fractures in low permeability rock., *Proceedings*, 6th ISRM Congress, Montreal, Canada, (1987).

Roels, S. M., Ott, H., and Zitha, P. L. J.: μ-CT analysis and numerical simulation of drying effects of CO_2 injection into brine-saturated porous media. *International Journal of Greenhouse Gas Control*, **27**,(2014), 146–154.

Roels, S. M.: Formation dry-out and injectivity impairment during CO_2 storage in saline aquifers, *Doctoral Thesi*s, University TU Delft, (2015).

Shahidzadeh-Bonn, N., Desarnaud, J., Bertrand, F., Chateau, X., and Bonn, D.: Damage in porous media due to salt crystallization. *Physical Review E : Statistical, Nonlinear, and Soft Matter Physics*, **81**, (2010).

Smith, M. M., Walsh, S. C., McNab, W. W., and Carroll, S. A.: Experimental investigation of brine- CO_2 flow through a natural fracture: permeability increases with concurrent dissolution/reprecipitation reactions. *Office of Scientific & Technical Information Technical Reports*, (2013).

Spycher, N., Pruess, K., and Ennis-King, J.: CO_2-H_2O mixtures in the geological sequestration of CO_2. I. Assessment and calculation of mutual solubilities from 12 to 100C and up to 600 bar. *Geochimica et Cosmochimica Acta*, **67**, (2003), 3015–3031.

Spycher, N., Pruess, K., and Ennis-King, J.: CO_2-H_2O mixtures in the geological sequestration of CO_2. II. Partitioning in chloride brine at 12-100C and up to 600 bar. *Geochimica et Cosmochimica Acta*, **69**, (2005), 3309–3320, 2005.

Tanaka, Y., Miyakawa, K., Fukahori, D., Kiho, K., and Goto, K. Survey of Flow Channels in Rock Mass Fractures by Resin Injection. *Proceedings*, ISRM International Symposium 2014, Sapporo, Japan, (2014).

Tang, Y., Yang, R., Du, Z., and Zeng, F.: Experimental study of formation damage caused by complete water vaporization and salt precipitation in sandstone reservoirs. *Transp. Porous Media*, **107**, (2014), 1–14.

Verma, A. and Pruess, K.: Thermohydrologic conditions and silica redistribution near high-level nuclear wastes emplaced in saturated geological formations, *J. Geophys. Res.*, **93**(B2), (1988), 1159– 1173.

Vogler, D., Amann, F., Bayer, P., and Elsworth, D.: Permeability evolution in natural fractures subject to cyclic loading and gouge formation., *Rock Mech. Rock Eng.,* **49**, (2016), 3463–3479.

Vogler, D., Walsh, S. D. C., Bayer, P., and Amann, F.: Comparison of surface properties in natural and artificially generated fractures in a crystalline rock*., Rock Mech. Rock Eng.*, **50**, (2017a), 2891–2909.

Vogler, D., Settgast, R. R., Annavarapu, C., Madonna, C., Bayer, P. and Amann, F.: Experiments and Simulations of Fully Hydro-Mechanically Coupled Response of Rough Fractures Exposed to High-Pressure Fluid Injection., *Journal of Geophysical Research: Solid Earth*, **123**(2), (2018), 1186-1200.

Wang, J., Tsang, C. F., and Sterbentz, R. A.: The state of the art of numerical modeling of thermo hydrologic flow in fractured rock masses., *Environmental Geology*, **4**, (1982), 133–199.

Wang, Y., Mackie, E., Rohan, J., Luce, T., Knabe, R., and Appel, M.: Experimental Study on Halite Precipitation During CO_2 Sequestration, *Proceedings*, International Symposium of the Society of Core Analysts, 27-30 September, Noordwijk, The Netherlands, (2009).

Xu, T. and Pruess, K.: Numerical Simulation of Injectivity Effects of Mineral Scaling and Clay Swelling in a Fractured Geothermal Reservoir, *Transactions - Geothermal Resources Council*, **28**, (2004).

Zeidouni, M., Pooladi-Darvish, M., and Keith, D.: Analytical solution to evaluate salt precipitation during CO_2 injection in saline aquifers, *International Journal of Greenhouse Gas Control*, **3**, 5, (2009), 600-611.

Zimmerman, R. W. and Yeo, I.: Fluid flow in rock fractures: From the Navier-Stokes equations to the cubic law. *Dyn. Fluids Fract. Rock*, **122**, (2000).